Scaffolded hiPSC liver organoids recapitulating bile duct tubulogenesis and periportal architecture.

Harini Rajendiran[1,8], Flora Luciani[2,8], Selma Serhrouchni[2,8], Anais Monet[2,8], Ong Hui Ting[1], Jin Zhu[1], Piyush Mishra [3,4], Marion Marchand[1,5,9], Geetika Sahni[1], Aditya Arora[1], Nai Mui Hoon Brenda, Matt s. Hepburn[6,7,8], Jiayue li [6,7], Alireza Mowla [6,7], Farzaneh Navaeipour [6,7], Brendan f. Kennedy[6,7,8], Virgile Viasnoff[1,5,9] *.

[1] *Mechanobiology Institute, National University of Singapore, 5a Engineering drive 1, 117411 Singapore*

[2] *CNRS@CREATE, 1 Create Way, #08-01 Create Tower, Singapore 138602*

[3] *Aix Marseille Univ, CNRS, I2M, Turing Centre for Living Systems*

[4] *Aix Marseille Univ, CNRS, Centrale Med, Institut Fresnel, Turing Centre for Living Systems*

[5] *Aix-Marseille Université, UMR 7325 Campus de Luminy 13009 Marseille, France*

[6] *BRITElab, Harry Perkins Institute of Medical Research, QEII Medical Centre, Nedlands and Centre for Medical Research, The University of Western Australia, Perth, Western Australia 6009, Australia*

[7] *Department of Electrical, Electronic and Computer Engineering, School of Engineering, The University of Western Australia, 35, Stirling Highway, Perth, Western Australia 6009, Australia*

[8] *Institute of Physics, Faculty of Physics, Astronomy and Informatics, Nicolaus Copernicus University in Toruń, Grudziadzka 5, 87-100 Torun, Poland*

[9] *BMC2, Centre National de la Recherche Scientifique, 5a Engineering drive 1, 117411 Singapore*

** Corresponding author. virgile.viasnoff@cnrs.fr*

Abstract:

Recapitulating the liver periportal area in vitro remains a major challenge due to its complex cellular composition and the coordinated development of both ductal and endothelial networks. Most existing bile duct organoid models fail to reproduce tubular extension and multicellular organization. Here, we present an approach that leverages biofunctionalized ECM micro-rods to scaffold the coordinated development of bile ducts, parenchymal cells, and vascular structures. Our system recapitulates key developmental stages, from the formation of the ductal plate to the emergence of elongated tubular ducts. We further demonstrate that this approach is scalable and amenable to quantitative analysis through label-free Optical Coherence Tomography combined with AI-driven 3D segmentation. We show that the ECM rod alone provides the biophysical cues to initiate the elongation of the bile ducts and the spatial structuration of the cellular organization, while the biofunctionalization with attached growth factors enhance the maturation and the connectivity of the biliary system.

Introduction:

The development of the liver periportal area is key to the functional organogenesis of the liver lobule. In the human embryo, it occurs between EW8 and EW10 and is spatially organized around the portal vein [1, 2]. Paracrine signaling via TGFβ and Notch from adjacent endothelial and mesenchymal cells induces the differentiation of embryonic hepatoblasts into cholangiocytes in the close vicinity of the vein. In turn, cholangiocytes develop the tubular network of intrahepatic bile ducts (IHBD) that closely scaffolds the portal vein network [3-6]. At EW10, hepatic arteries begin to develop in the vicinity of the IHBD, reportedly in response to VEGF signaling from cholangiocytes [7, 8]. Meanwhile, the remaining parenchymal hepatoblasts differentiate into hepatocytes. Local paracrine signaling, acting over just a few cell diameters, is paramount to the spatial and temporal coordination of the three tubular

networks (portal vein, hepatic arteries, and intrahepatic bile ducts), with each network signaling for the development and maintenance of the others.

Our current understanding of the portal triad is largely based on homologies between murine and human development. Human liver organoid models have focused either on the generation of complex liver bud surrogates that reproduce the diversity of cell types [9-11], irrespective of their spatial organization, or on the development of bile duct organoids from induced or primary cholangiocytes [12-18]. In all cases, cellular differentiation in organoids is controlled by a sequence of homogeneous soluble growth factor treatments and by embedding them in an extrinsic (culture within) extracellular matrix scaffold. Under such conditions, cholangiocytes can mature into large spherical cysts comprising a single-cell monolayer. More advanced techniques, like 2D patterning and hydrogel microparticles, have enabled spatiotemporal regulation of hepatoblast fate, but they often lack ECM-derived cues and topological drivers that are critical for cytoskeletal reorganization during tissue formation [19-21]. Whereas the osmotic growth of cholangiocytes cysts most often leads to spherical structures, recent studies using 2D patterning on fibronectin substrates have demonstrated the creation of cholangiocytes tubes based on a non-physiological self-wrapping cell layer mechanism [22]. Primary adult (and not embryonic) cholangiocytes placed in an optimized ECM environment have been shown to create branched bile duct–like tubules [23]. Lastly, the co-culture of hepatoblasts around endothelial cells adhered to a cylindrical rod led to the formation a periportal area like structure. Efforts to incorporate portal vein cues have generated bile ducts in proximity to the signaling center, but these systems remain low-throughput and highly variable due to the undefined nature of the factors secreted by portal vein cells [24].

Since the liver portal triad development results principally from local juxtacrine and paracrine signaling around the portal vein scaffold, we reasoned that the classical approaches in organoid culture using soluble growth factors stimulation might lack important components necessary to the portal triad development. In this paper, we used rod-like scaffolds biofunctionalized with growth factors to mimic the paracrine signaling that elicits the initial differentiation of hepatoblasts along the portal vein. In contrast to the conventional approaches requiring soluble cues and ECM embedding, our system recapitulate the periportal organogenesis from hiPSCs capturing the coordinated emergence of ductal, parenchymal and vascular compartments. It reproduces a large fraction of the cellular diversity and the temporal sequence of development including the formation of a tubular bile duct. supports intrinsic self-organization of the portal triad architecture. To enable the dynamic and non-invasive morphological assessment of these structures, we developed a 3D imaging pipeline using Optical Coherence Tomography (OCT), allowing the scalable quantification of the ductal architecture and its morphogenesis.

Results:

Scalable biofunctionalized 3D scaffolds mimicking portal vein cues.

To recreate the spatial organization of cellular interactions present along the embryonic portal vein, we engineered a series of biofunctionalized scaffolds designed to deliver juxtacrine and paracrine cues (Notch, TGFβ, and geometry) mimicking the instructive role of the mesenchyme and endothelial lining of the vein in vivo (Figure 1a). As surrogates for the embryonic portal vein, we engineered Gelatin Methacrylate (GelMa) rods with physiological dimensions (0.3 × 1 mm) and addressable combinations of growth factors chemically conjugated to the extracellular matrix (ECM) (Figure 1b, Materials and Methods). Molding the

rods in long Polyethylene tubes (*500* µm *internal diameter*) ensured consistent dimensions: diameter of 400 µm (after swelling) and lengths ranging between 0.8 to 1.5 mm after manual chopping (**Figure 1c, Supplementary Figure 1a**). The elastic modulus of the scaffolds measured using atomic force microscopy (AFM) averaged around 3.6 kPa, in agreement with the physiological range (**Supplementary figure 1b**). We coupled the growth factors (GF) to the rods using their heparin-binding domain when present. For those lacking this domain (Jagged1-FC), we employed protein G based coupling to enable targeted binding (Figure 1b). In all cases, we confirmed that the coupling was localized at the rod surface (Figure 1c). Performing ELISA on the supernatant of the incubation medium, we quantified that up to 46% of the soluble growth factors from the initial bound to the rods (**Material and Methods**) corresponding to an average of 761 pg of Activin a per rod likely saturating the biding sites. This immobilization efficiency was consistent across different ligands and did not vary with longer washing period demonstrating that growth factors are not released from the rods (**Figure 1c**, **Supplementary 1b**). We prepared the biofunctionalized rods in high-throughput batches and seeded individually into U-bottom 96-well plates to scaffold the development of our human Periportal area organoids (hPPAo) (**Materials and Methods, Figure 1c)**.

To derive the hPPAo from hiPSCs, we first generated embryonic hepatoblasts from hiPSCs following a previously established protocol by Sampoziotis *et al* 2017, as summarized in [12]. **Figure 1d** (**Materials and Methods**). After 13 days of stepwise differentiation the vast majority of cells in the 2D culture expressed liver hepatoblasts markers (AFP and HNF4A), with a small fraction additionally expressing cholangiocyte markers including Cytokeratin 7 (CK7) and SOX9 (**Supplementary figure 1c**). We further tested the bi-potency of the hepatoblasts by differentiating them into hepatocytes and cholangiocytes on adherent culture following [25] (**Supplementary figure 1d**). To initiate hPPAo formation, we harvested as single cell the 2D culture and seeded them on the biofunctionalized scaffolds in 96-well low attachment plates at a density of 50,000 cells per rod (**Figure 1d**). The seeding day sets the reference time point of the protocol Day 0 (D0). This optimized seeding density ensures a complete coverage on of the rod surface by several cell layers, without extensive cell death and the presence of a single organoid per well (**Material and Methods**). It was key to the success of the further development of the organoid. From D0 onwards, the hPPAo grew in a maintenance medium (RPMI medium) deprived of any soluble growth factors or ECM components. We hence guided the hPPAo maturation and organisation exclusively by the biophysical and biochemical cues provided by the scaffolds as well as by the factors (growth factor and extra cellular matrix) self-secreted by the cells. In the rest of the paper we study three combinations of biofunctionalization: the rods without any Growth factors, or biofunctionalized with Activin A and FGF10 or with Activin A and FGF10 and Jag1.

As differentiation progressed, cells spread uniformly covering the rod surface by D1. After 6 days, the hPPAo developed mm sized elongated lumens (**Figure 1d** (D6)). The tubular structures exhibited a pulsatile behaviour (**Supplementary Video 1**), indicative of an ion secretion activity into the luminal cavity.

***In vivo* like maturation of elongated bile ducts in hPPAo**

We immuno-stained hPPAo grown on rods biofunctionalized with Activin A and FGF10 for early cholangiocytes markers (Sox9, E-cadherin) and the hepatoblasts marker HNF4a. Confocal imaging (10X objective) on day 1 (D1) revealed a continuous, multi-layered coating on the rods reaching a thickness of 4 to 6 cell layers (**Figure 2a).** The innermost layer in contact with the rod segregated into two distinct populations of complementary discontinuous monolayers comprising either cholangiocytes-like cells (Sox9+, E-cadherin+) or the hepatoblasts (HNF4a+) (**Figure 2a**, **Supplementary Figure 2a).** Surrounding this interface, we observed a large fraction of HNF4a cells extending radially outwards up to 20 cell width from the rod, resembling the embryonic parenchyma **.** This spatial organisation is much akin to the development of the ductal plate around the portal vein (Week 8 of dev) surrounded by the embryonic parenchyma [1, 5].

Note, however that sparse cholangiocytes differentiation also occurred at distant locations away from the rod, particularly in regions with thicker parenchymal density. This "un-scaffolded" differentiation likely resulted from the presence of cholangiocytes precursors in the initial hepatoblast population at D0 following the 2D culture (see Discussion).

Together, our findings suggest that localized juxtacrine differentiating signals (Gelma rods + Activin a + FGF10) provided by the rods are sufficient to faithfully phenocopy the early stages of ductal plate formation.

Unlike typical *in vitro* cystic bile ducts comprising a single layer of cholangiocytes, the BEC self-organised into tubes between the rods and the surrounding parenchyma at Day 6. Immunostaining confirmed that these were *bona fide* bile duct with cholangiocytes forming the luminal lining expressed E-cadherin, CK7 and SOX9 while downregulating the progenitor markers HNF4a, Albumin, and SOX17 (**Figure 2b-c**) (**Figure 2c**). The lumens displayed varying morphologies including both elongated lumens and compartmentalized tubular segments (**Figure 2b**). Cells in the outer tubular layer were cuboidal with lateral E-cadherin expression (**Figure 2b**) while those in the transverse layers were more elongated (**Figure 2b**).We further observed a clear apico-basal polarity (apical localization of the tight junction zonula occludens-1 (ZO-1) and ciliary localizing proteins ADP ribosylation factor like GTPase 13B (ARL13B)) of the ductal epithelial cells, with a continuous laminin rich basal layer delineating them from the surrounding parenchyma (**Figure 2e**, **Supplementary figure 2b**). Other transport proteins such as sodium potassium ATPase and secretin receptors (**Supplementary Figure 2b**) also polarized apically, confirming the secretory activity of the bile ducts.

The cellular diversity recapitulates that of the liver peri-portal area.

To complement immunolabeling-based cell identification, we performed single cell RNA sequencing (10000 cells, approximately 5000 genes) (**Material and Methods**) on D6 hPPAo grown of rods biofunctionalized with Activin a and FGF10.

We mapped to embryonic liver cell types using gene lists (Material and Methods) from based on the reported data [26-30] at a resolution of 10 clusters (**Figure 3a**).

Single cell transcriptomics revealed four transcriptionally distinct hepatoblast clusters : eHB enriched for early markers (EFNB2, TTC6, SERPINA1), mHB expressing migratory markers (GATA4, CDH2, FN1, and GPC3), pHB other undergoing proliferation, and fHB characterized by strong expression of cell-cell adhesion proteins (CDH1) as well as foetal markers such as ONECUT2, HHEX, PROX1, and NPW (**Figure 3a**). From these hepatoblast, emerged the liver epithelial cells the cholangiocytes and the hepatocytes (**Supplementary figure 3a-b**). Notably, the cholangiocytes cluster BEC expressed several matrix remodelling proteins (VIM, COL1A1, COL2A1, COL3A1, LAMB1, CTHRC1, and LUM), suggestive of remodelling stages (**Supplementary figure 3a**). Supporting this, gene ontology studies revealed significant enrichment for biological process associated with epithelial tube morphogenesis (**Supplementary figure 3d**). In parallel, the hepatocytes HP expressed a spectrum of metabolic and developmental genes with the most mature ones expressing high levels of genes associated with lipid metabolism (APOA, APOB, APOE, APOC), blood coagulation (F10, FGA, SERPINA6, SERPIND1), detoxification (GSTA1, GSTA2), glucose and fatty oxidation (PDK4, CPT1A, and SLC27A5), plasma protein production (TTR, AHSG), fatty acid metabolism (FABP1) and oxidation reduction process (CYP2D10, SORD, HSD17B2) (**Figure 3a**, **Supplementary figure 3a**). The most fetal hepatocytes fHP expressed similar metabolic functions but still retained their fetal features such as PROX1, HHEX and DLK1. Despite the maturation, immunostaining did not reveal the presence of any bile canaliculi, suggesting that the hepatocytes have not reached their polarized maturation stage (**Supplementary figure 3a**). The degree of immaturity of Cholangiocytes was confirmed by the lack of expression of ABCB1(MDR1) and ABCC2(MRP2) , and, for hepatocytes, the expression of cytochrome p450 genes (**Supplementary figure 3a-c**). Besides the endoderm derivatives, the hepatic stellate cells also resolved into two subclusters among which one is in activated state aHSC expressing (COL1A1, COL3A1, COL6A3, ITGA8, MMP2, ZEB2, EPHA3, MFAP4, and TNNI1) and pHSC in proliferative state (UBE2C, CDC20, CENPF, and SOX17). Endothelial cells expressing PECAM, KDR, GNG11, CDH5 and NOTCH1were also present indicating the presence periportal mesodermal cells types in the organoids.

We selected the most discriminative genes of each cluster and use them to identify their spatial organization by confocal immunofluorescence imaging. Elongated bile duct and the hepatoblasts l predominantly been localized in the vicinity of the rods (**Figure 3 b-c**). Whereas, albumin-positive hepatocytes localized preferentially at the periphery of the organoids (**Figure 3 c**). The hepatic progenitor population, SOX17^{+} endoderms , consistently lined the bile duct lumens, with some proliferating sub-populations identified by Ki-67 (**Figure 3c**). Hepatic Stellate Cells (NCAM^{+}) were distributed across the parenchymal regions occasionally capping bile duct lumens (**Figure 3c**). The endothelial cells (VE-cad+) distributed into two distinct regions: either as a layer surrounding the rods or as an epithelium lining oblate lumens. The first population can be found intercalated between the rods and the elongated bile duct, positioned on the other side of the laminin rich basal membrane, hence displacing the bile ducts outwards from the rod surface. The second population (VEGF+ **Supplementary figure 4a-b**) formed epithelial luminal structures in the parenchymal regions, often adjacent to the bile ducts. Together these spatial arrangements shared strong morphological resemblance with the *in vivo* portal triad configuration. (**Figure 3c**). Both populations displayed transcriptional markers for

veins and arteries alike. However they were indistinguishable from their transcriptional profile, suggesting a common progenitor identity. We did not observe the expression of STAB2 and CLEC4G which are markers of sinusoid endothelium. The induction of endothelial population in our system could originate from paracrine VEGF signalling from cholangiocytes, reminiscent of the *in vivo* developmental process. While cholangiocytes actively expressed angiogenic factors (VEGFA and ANGPT1), other cell types equally contributed to their bulk concentration (**Figure 3e, Supplementary figure 4c**). Interestingly, the corresponding receptors (KDR and FLT1) were only restricted to the endothelial clusters, suggesting an spatial organisation based on paracrine signalling and not large scale growth factor gradient (**Figure 3d, Supplementary figure 4d)**. Unexpectedly the endothelial cell expressed the endoderm marker SOX17 instead of the mesoderm markers. Similar expression profile was already reported for hIPSCs derived liver organoids and *in vivo*.

The transcriptional analysis at D0 just after the phase of 2D culture (**Figure 3d-e**) displayed a cell types profile comparable to that of D6 although with different the relative proportion between cell types and different maturation stages (**Figure 3f, Supplementary figure 4d**). The D0 hepatic endoderm disappeared at day 6 (fHP, fHB) with the expansion of Hepatocytes (HP) and Cholangiocytes (BEC) as demonstrated by pseudo time analysis (**Supplementary Figure 3b**). Stellate cells matured and Endothelial cells extended. These shifts in populations occurred in the absence of any exogenous soluble growth factors and that the differentiation results exclusively from self-organized secretion of differentiation factors and extracellular matrix. It then questioned the role of the biofunctionalized rod in the hPPAo development.

Juxtacrine signalling from the scaffold governs bile duct phenotypes.

We next investigated how Notch and TGFβ signalling affects the morphologies of bile ducts in hPPAo. Both pathways have been extensively studied for their roles in the bile duct developmental process. [8, 30, 76-80]. While TGFβ is known to regulate biliary differentiation and Notch acts downstream to drive bile duct morphogenesis, conflicting results exist as perturbation experiments using small molecules produce off-target effects in multicellular systems [6, 51, 80, 158]. Moreover, how these signalling pathways can be spatially controlled in *in vitro* systems to guide tissue organisation is also under active investigation.

We thus compared the developmental outcomes of the hPPAo under geometrical and ECM scaffolding only (GelMA rods without growth factors) or in the presence of paracrine differentiating growth factor signals (AF rods : GelMA rods biofunctionalizated of Activin A and FGF10) or adding more morphogenetic signalling (JAF rods: GelMA rods functionalized with Jag 1, Activin A and FGF10).

At D1, in the absence of biofunctionalization (no Growth factors on the rod), cholangiocyte differentiation occurred homogeneously in the parenchymal region (hepatoblasts) surrounding the rods (**Supplementary figure 5a**). Focusing on the first cell layer at the rod interface, reveals a sparse differentiation of hepatoblasts into cholangiocytes (**Figure 4a, Supplementary figure 5b**). As described in **figure 2a**, functionalization of Activin A and FGF10 on the rod surface enhanced the local differentiation of cholangiocytes into a discontinuous monolayer (**Figure 4a)**. Strikingly, the immobilization of Jag 1 (Notch signalling) to Activin A and FGF10 further

enhanced the localization of the differentiation at the interface resulting in the formation of a continuous sheath around the rod (**Figure 4a**, **Supplementary figure 5c**) . Addition of Jag 1 helped the localisation and the structuration of the morphogenesis of the organoids. **Figure 4a-b** show the quantification of the surface differentiation using a radial projection of the image of the first cell layer (**Supplementary figure 5a**) at the rod surface. The results indicate an increase in the differentiation levels from 34% in control samples to 46% in Activin a and FGF10 reaching up to 61% in Notch activated samples (**Figure 4b**). Moreover, the introduction of notch pathway reduced the number of discrete cholangiocyte clusters and increased their average area (**Figure 4b**).

At D6, UMAP clustering of scRNAseq data comparing all three conditions (**Figure 4c**) did not reveal any measurable difference in term of cellular composition. This result further suggests that the presence of grafted growth factors on the rods does not influence the cellular diversity that is likely to originate from the self-induced differentiation of the original cell population at D0. In particular, the cholangiocytes across all conditions expressed key markers such as Cytokeratin 7, SOX9 and E-cadherin, with a concurrent reduction in hepatoblast and hepatocyte marker albumin (**Supplementary figure 6**). It provides guiding cues to enhance the maturation and structuration programs of the cellular types. Notably, the induction of Notch led to the expression of MDR1, an ATP-dependent efflux pump crucial for cholangiocyte protection, suggesting a role for notch signaling in cholangiocyte maturation (**Supplementary figure 6a**). However, the bile ducts were unable to transport the bile acid analogue, Cholyl lysyl fluorescein (CLF), suggesting they have not achieved full functional capability (**Supplementary figure 6a-b**).

Despite similar cellular composition across different conditions, hPPAos presented salient differences in bile duct morphology. In control samples, cholangiocytes self-organized to form oblate lumens with minimal elongation (**Figure 4d**). With Activin A and FGF10 bile ducts appeared as elongated interconnected lumen that maintained intact epithelial walls between adjacent structures (**Figure 4d**). Notably, the presence of Jag 1 enhanced this remodelling process, characterized by the coalescence of lumens into long continuous ducts along the rod axis (**Figure 4d**). This progressive tubular formation, achieved with minimal fusion events is reminiscent of *de novo* bile duct morphogenesis. Our results confirm *in vitro* the direct influence of Notch signalling on the ductal plate remodelling.

Quantification of bile duct tubulogenesis by Optical coherence tomography.

The assessment of the bile duct morphologies using confocal microscopy (Material and Methods) required prolonged imaging (more than 10 hours per organoid at 10X objective) yielding a very low throughput and limited imaging depth (typically up to 200µm in the hPPAo). Although distinct lumen morphologies were distinguished visually, the method lacked standardized pipelines for unbiased detection and quantitation . To overcome these limitations, we used Optical Coherence Tomography (OCT), a label free imaging technology that leverages on refractive index changes between the lumens and the surrounding tissues to generate 3D high contrast images (**Figure 5a-b**). OCT offers sufficient depth penetration (up to to 2mm) in thick tissues with high spatial (4.8 µm) and temporal resolution (10 s for *in toto* imaging of the

organoid). It hence enabled rapid 3D volumetric imaging of lumens. (**Supplementary figure 7**). We performed extensive imaging of 96 well plates on a custom made OCT imager (**Material and Methods**). We developed a semi-automated pipeline for the extraction and analysis of the lumen morphological features (**Supplementary Figure 8**). The entire pipeline process is described in **Supplementary information**. Briefly (**Figure 5c**), we used simple pre-processing schemes (denoising and contrast enhancement) on the raw images. We used a custom developed algorithm (**Material and Methods**) to extract the mask of the rod volume (coupling water-shading and a-priori knowledge of the rod shape). Using sparse 2D planes of the organoids images, we then trained Ilastik (running on an ImageJ environment) to segment the lumen cavities from the cellular areas. Batch processing for the whole z-stacks of one organoid batch was then possible. However, in our experimental condition the training had to be performed for each batch due to the experimental variability of the imaging noise. A 3D volume representation of each hPPAo was obtained from the segmented image stacks estimation of the overall hPPA shapes) in IMARIS (Andor). The extraction of the morphological features of each segmented luminal cavities was performed using IMARIS analysis (**Figure 5c**). The smoothing parameters to merge adjacent lumens were adjusted by comparison the raw images to the segmented ones. They were kept identical for all hPPAo batches. The performances of the pipeline are described in supplementary information.

We then performed k means clustering on 6 principal morphometric parameters of the lumens to classify them in an unbiased manner (**Supplementary figure 9**). We first performed clustering pooling three different time points (D4, D5, D6) for rods biofunctionalized with Activin A and FGF10. The unsupervised clustering revealed 4 different groups: SL for Small Lumens. OL for Oblate lumens , ST for Short Tubes and LT for long Tubes. The cluster name correspond to the visual impression of the lumens associated with each clusters (can we do better than that?).The LT cluster counts few number lumens and no more than one per organoid since they represent tubular structure that span almost the entire length of the rod and that are structurally similar to the very long bile duct that we observed by confocal microscopy. **Figure 5d** reveal the progressive development of long tubes and the gradual loss of oblate lumens, consistent with the idea of a gradual fusion of individual cystic bile ducts into a single long tube. These fusion events are also characterized by the high resolution (20µm) OCT live images (**Figure 5a**) were we detected the presence of small gaps between adjacent luminal cavities. We also observe that SL and OL are statistically far from the rod surface whereas the LT are in close vicinity of the rod. Note that the distance to the rod is not a parameter included to define the clusters. Taken together, OCT imaging allows us to detect the morphologies of the cavities. Clustering allows detecting the long tubular bile ducts. We were not able though to morphologically discriminate short bile ducts from endothelial cavities that cluster together in the ST clusters.

We then assessed the alignment of the lumens along the main axis of the rods. We calculated the angle between the rod axis and the main axis of each lumen (**Figure 5e**). LT and ST shows a clear orientation of the luminal cavity along the rods. OL and SL were more isotopically distributed with some bias orthogonally to the main axis. Note that the angle is not part of the

clustering criteria. It shows that the geometrical cues provided by the rod orient the development of the bile doc, that does not spiral around the rod but rather develop directionally.

We finally performed k means clustering to compare Activin A/FG10 and Jag1/Activin A/FGF10 conditions (**Figure 5g, Supplementary figure 10**). It confirmed the existence of 4 clusters that matched the characteristics of those found previously.

Discussion:

In this work, we adopted an original strategy to create periportal organoids (hPPAo) that follow a developmental trajectory mimicking in vivo liver development. We first differentiated hIPSCs in 2D using a protocol that generated a mixed population of liver and mesenchymal progenitors. We then used a biofunctionalized ECM-based rod to guide the local organization of these diverse cell types into a major bile duct surrounded by liver parenchyma and endothelial lumens. The process relies entirely on the biophysical and biochemical cues provided locally by the rods. After 7 days of maturation, we observed the formation of an elongated bile duct spanning almost the entire length of the rod, originating from a ductal plate–like organization present on day 1. Although lacking specific arterial or venous markers, the endothelial structures organized in a stereotypical manner, eventually occupying the space between the rod and the bile duct and forming luminal structures around it. In its current form, the organotypic assembly also displays a heterogeneous parenchyma containing hepatic precursors, immature hepatocytes, and stellate cells. We also observed numerous spherical BEC lumens in the thicker regions of the parenchyma, which tend to "erode" during development, leading to large sections of the organoid detaching—primarily during media changes. Due to this erosion issue, we were unable to culture these organoids beyond day 7. This limitation could likely be addressed by embedding the hPPAo in an external hydrogel scaffold, though such an intervention would also alter tissue organization and require precise ECM tuning, which we reserve for future studies. Our bioscaffold approach is scalable and compatible with parallel culture formats such as 96-well plates. We leveraged this by developing a semi-automated screening method using Optical Coherence Tomography (OCT) to classify luminal cavities. This work serves as a proof of concept demonstrating how scaffolded hPPAo culture, OCT imaging, and quantitative analysis can be integrated into a pipeline. Further work is needed to fully automate image acquisition, as the current analysis still depends on experimentalist input. One area for improvement is the development of an objective criterion to determine whether adjacent lumens are connected, which remains a limitation of our current analysis and requires experimental validation. Since high-resolution OCT imaging provides clear visualization of connecting gaps, we are developing AI-based methods to recognize such features in 3D, enabling reliable discrimination between adjacent and truly connected bile ducts. Enhancing image contrast consistency across batches and training Ilastik on larger datasets will also reduce the need for frequent retraining of the lumen segmentation algorithm.

The mechanism of intrahepatic bile duct (IHBD) tubulogenesis remains an open question, with proposed mechanisms including cord hollowing, lumen fusion, and elongation by proliferation [6, 31-34]. We propose that our approach offers a powerful tool to elucidate key developmental processes in the liver. In the hPPAo model, tube formation appears to occur through the fusion of multiple small lumens, driven primarily by spatial proximity and without evidence of cell proliferation. Although current technical limitations prevent real-time tracking of tube dynamics, future advancements in imaging technology will likely enable a more detailed investigation of the tubulogenesis process [35, 36]. While it is well established that TGFβ

signaling is essential for ductal plate formation and Notch signaling plays a role in late-stage remodeling, the function of Notch in the early stages remains unclear. In disease contexts, lumens often develop into cystic or oblate structures that fail to elongate into tubes, yet the molecular pathways and microenvironmental changes responsible for this failure are still poorly understood. Furthermore, the mechanical requirements of bile duct development have often been overlooked, despite increasing evidence suggesting that mechanical cues play a crucial role in guiding tube formation. Our system provides a complementary platform to address these outstanding questions.

The results indicate that TGFβ signaling is essential for ductal plate formation and that its effects are amplified in the presence of active Notch signaling. While topological guidance is required during bile duct remodeling stages, it must act in concert with paracrine cues—whose absence can lead to failure in remodeling into proper tubular structures. Our findings suggest that no single factor is sufficient to drive this remodeling, as the organoids frequently exhibited polycystic morphologies with multiple dilated cavities in three dimensions. We speculate that these phenotypes may result from cell sorting behaviors among differentiated cells expressing high levels of E-cadherin, potentially specific to our experimental setup. As such, optimizing the proportion of differentiated cells is critical to promoting proper connectivity and reducing off-target effects in static culture conditions. In vivo, the postnatal enlargement of the portal vein likely mitigates these sorting behaviors by positioning lumens on either side of the vein. At present, our system lacks the ability to reproduce such dynamic anatomical changes, but future developments in microfluidic technology could help mimic these transitions, offering a more accurate model for intrahepatic bile duct (IHBD) development.

Acknowledgments:

VV acknowledges support from MBI core funding, CALIPSO grant NRF2019-THE002-0007, and Chaire d'Excellence AMIDEX 2ORGASRH. VV acknowledges the kind gift of the patient derived hIPSCs from Dr S.Rashid Tamir (Imperial College London).

AUTHORS CONTRIBUTIONS

HR and VV designed the research. HR, MM, GS performed the biological experiments. FL, SS, AM, OHT, PM performed the image analysis. HR and AA engineered the rod approach. HR and JZ performed bioinformatic analysis for all the single-cell RNA-seq data and LC helped in scRNA-seq data analysis. NMHB, MH, JL, FN, BK provided technical and assistance support for the OCT imaging. HR and VV wrote the manuscript.

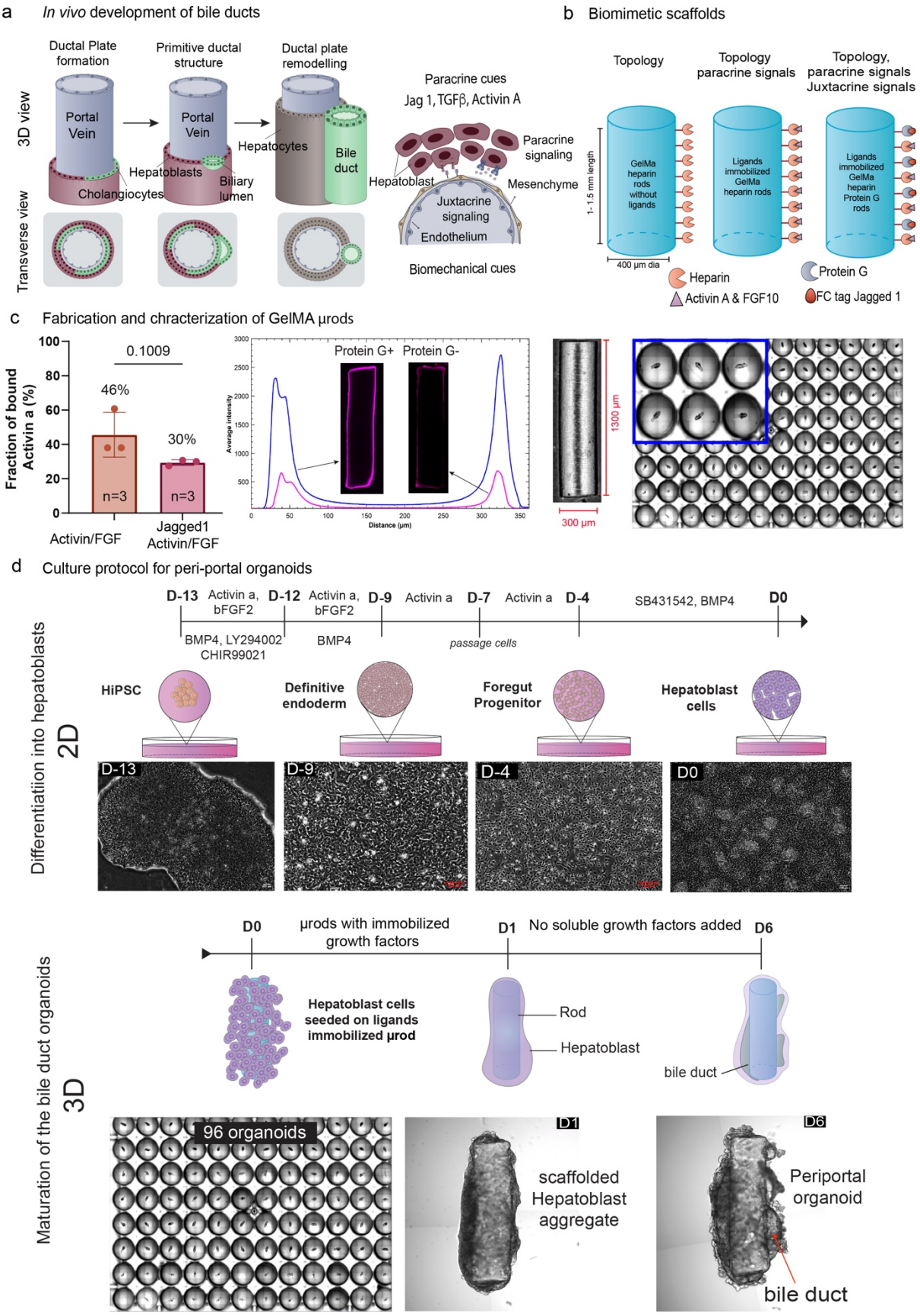
a
In vivo development of bile ducts
Ductal Plate formation
Primitive ductal structure
Ductal plate remodelling
3D view
Transverse view
Portal Vein
Portal Vein
Hepatocytes
Bile duct
Hepatoblasts
Biliary lumen
Cholangiocytes
Paracrine cues
Jag 1, TGFβ, Activin A
Paracrine signaling
Hepatoblast
Mesenchyme
Juxtacrine signaling
Endothelium
Biomechanical cues
b
Biomimetic scaffolds
Topology
Topology paracrine signals
Topology, paracrine signals Juxtacrine signals
GelMa heparin rods without ligands
Ligands immobilized GelMa heparin rods
Ligands immobilized GelMa heparin Protein G rods
1-1.5 mm length
400 µm dia
Heparin
Activin A & FGF10
Protein G
FC tag Jagged 1
c
Fabrication and chracterization of GelMA µrods
Fraction of bound Activin a (%)
0.1009
46%
30%
n=3
n=3
Activin/FGF
Jagged1 Activin/FGF
Protein G+
Protein G-
Average intensity
Distance (µm)
1300 µm
300 µm
d
Culture protocol for peri-portal organoids
D-13
Activin a, bFGF2
D-12
Activin a, bFGF2
D-9
Activin a
D-7
Activin a
D-4
SB431542, BMP4
D0
BMP4, LY294002 CHIR99021
BMP4
passage cells
Differentiatiion into hepatoblasts
2D
HiPSC
Definitive endoderm
Foregut Progenitor
Hepatoblast cells
D-13
D-9
D-4
D0
D0
µrods with immobilized growth factors
D1
No soluble growth factors added
D6
Maturation of the bile duct organoids
3D
Hepatoblast cells seeded on ligands immobilized µrod
Rod
Hepatoblast
bile duct
96 organoids
D1
scaffolded Hepatoblast aggregate
D6
Periportal organoid
bile duct

Figure 1

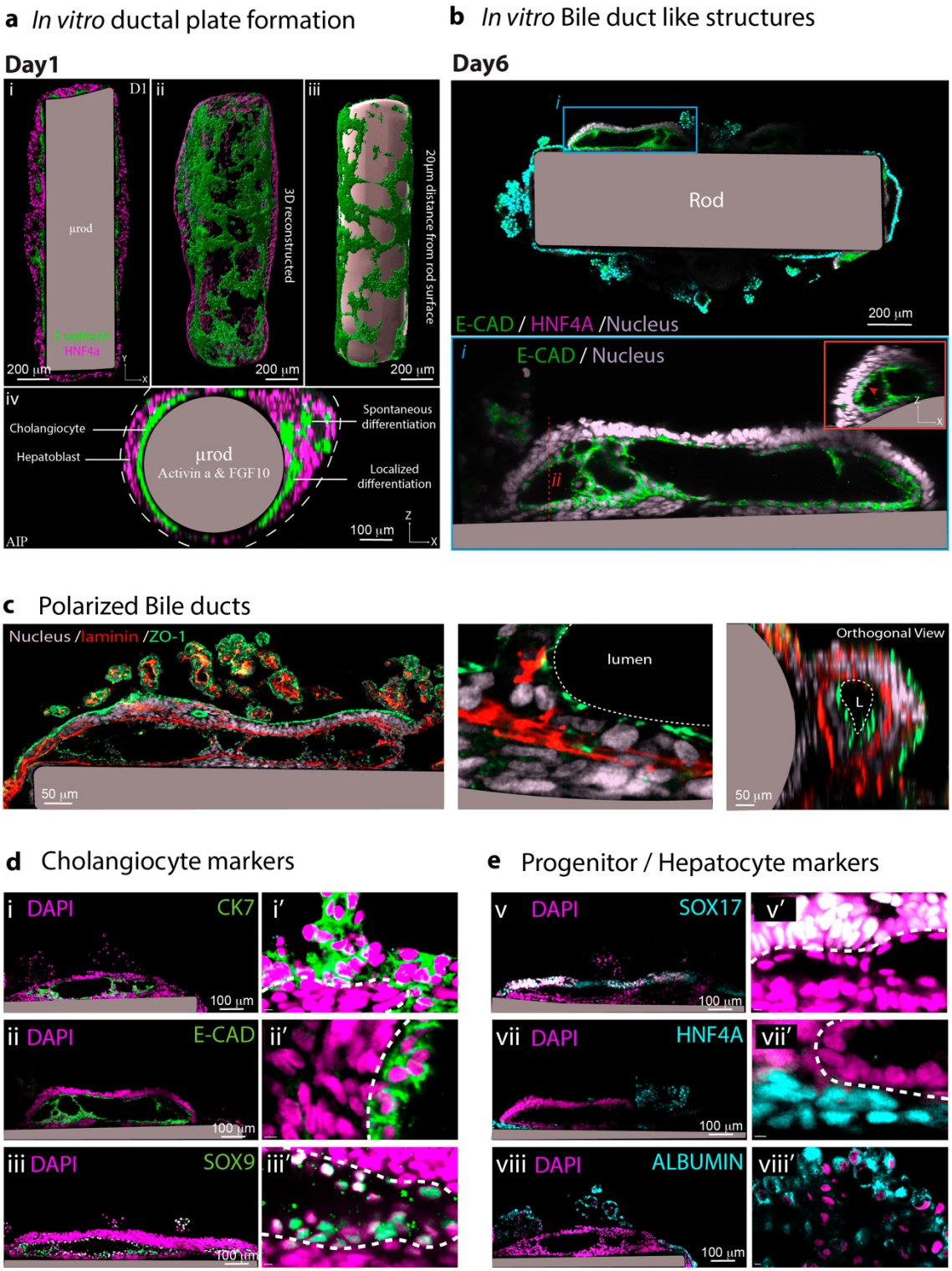
a In vitro ductal plate formation
b In vitro Bile duct like structures
Day1
Day6
D1
μrod
E-cadherin
HNF4a
200 μm
3D reconstructed
20μm distance from rod surface
Cholangiocyte
Hepatoblast
Activin a & FGF10
Spontaneous differentiation
Localized differentiation
100 μm
AIP
Rod
E-CAD / HNF4A /Nucleus
E-CAD / Nucleus
c Polarized Bile ducts
Nucleus /laminin /ZO-1
50 μm
lumen
Orthogonal View
d Cholangiocyte markers
e Progenitor / Hepatocyte markers
DAPI
CK7
E-CAD
SOX9
SOX17
HNF4A
ALBUMIN

Figure 2

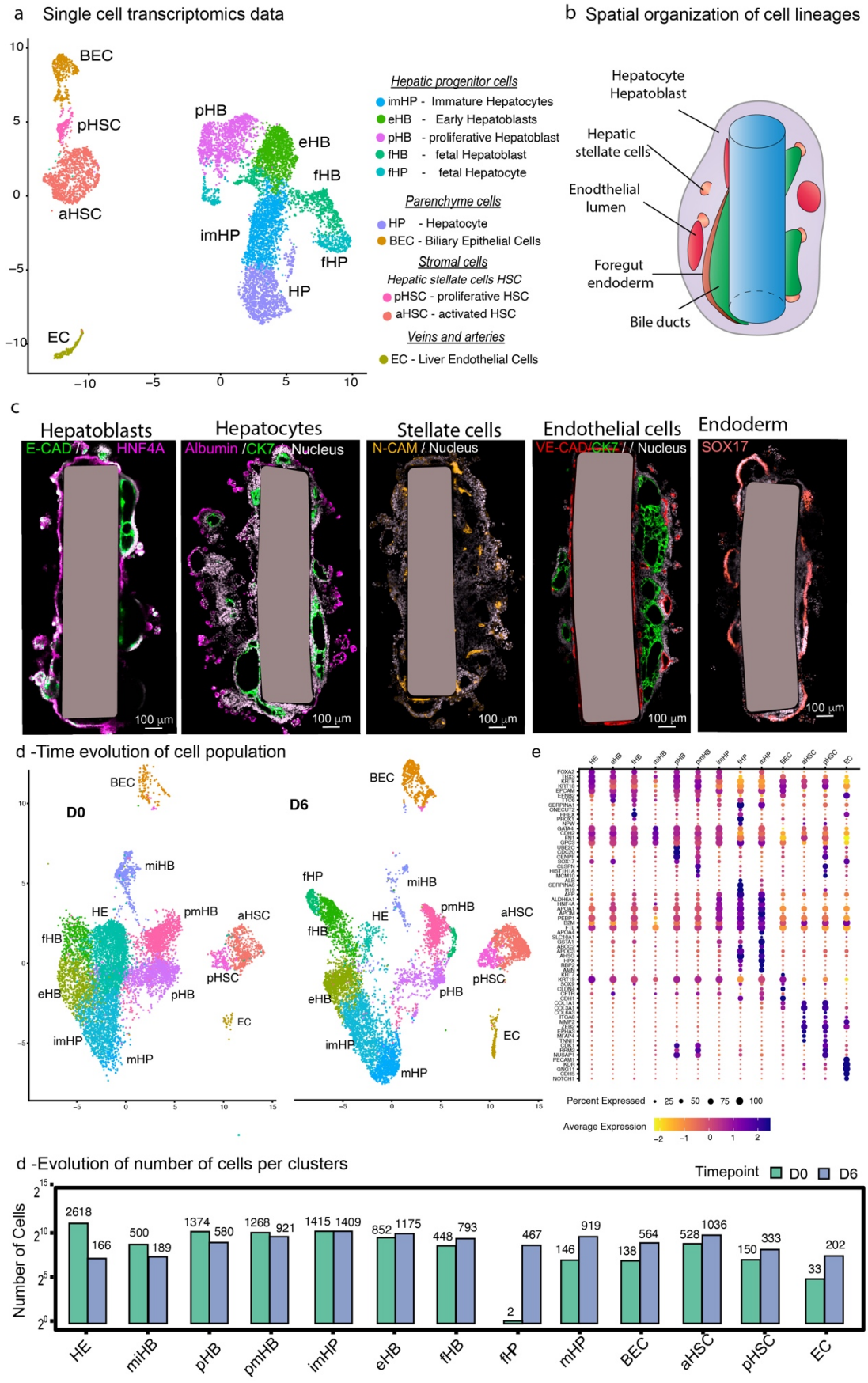
a Single cell transcriptomics data
b Spatial organization of cell lineages
BEC
pHSC
aHSC
EC
pHB
eHB
fHB
imHP
fHP
HP
Hepatic progenitor cells
imHP - Immature Hepatocytes
eHB - Early Hepatoblasts
pHB - proliferative Hepatoblast
fHB - fetal Hepatoblast
fHP - fetal Hepatocyte
Parenchyme cells
HP - Hepatocyte
BEC - Biliary Epithelial Cells
Stromal cells
Hepatic stellate cells HSC
pHSC - proliferative HSC
aHSC - activated HSC
Veins and arteries
EC - Liver Endothelial Cells
Hepatocyte Hepatoblast
Hepatic stellate cells
Enodthelial lumen
Foregut endoderm
Bile ducts
c
Hepatoblasts
E-CAD / HNF4A
Hepatocytes
Albumin /CK7 / Nucleus
Stellate cells
N-CAM / Nucleus
Endothelial cells
VE-CAD/CK7 / / Nucleus
Endoderm
SOX17
100 µm
d -Time evolution of cell population
D0
D6
HE
miHB
pmHB
aHSC
pHSC
pHB
mHP
e
Percent Expressed
Average Expression
d -Evolution of number of cells per clusters
Timepoint D0 D6
Number of Cells
2618 166
500 189
1374 580
1268 921
1415 1409
852 1175
448 793
2 467
146 919
138 564
528 1036
150 333
33 202
HE miHB pHB pmHB imHP eHB fHB fHP mHP BEC aHSC pHSC EC

Figure 3

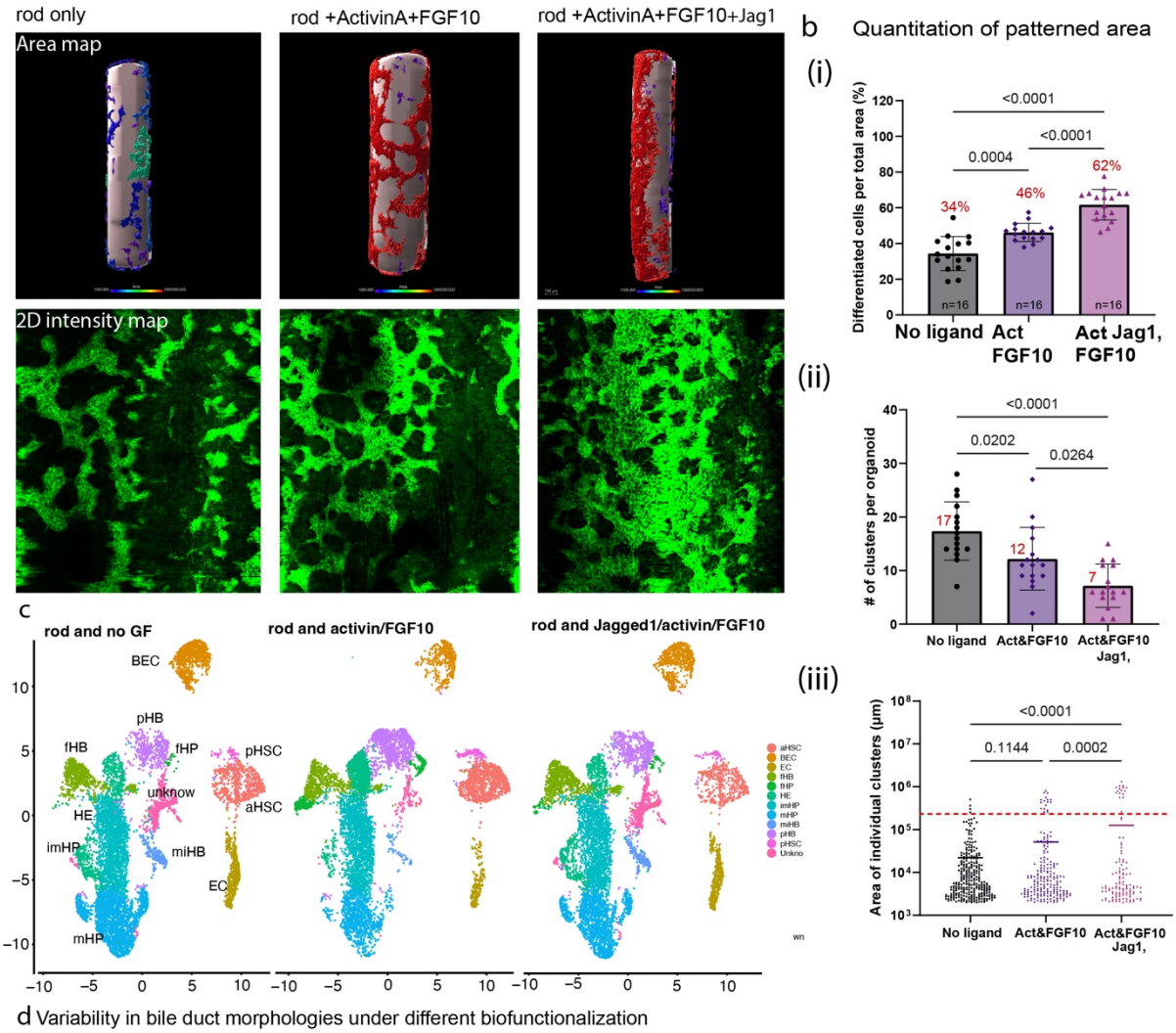

d Variability in bile duct morphologies under different biofunctionalization

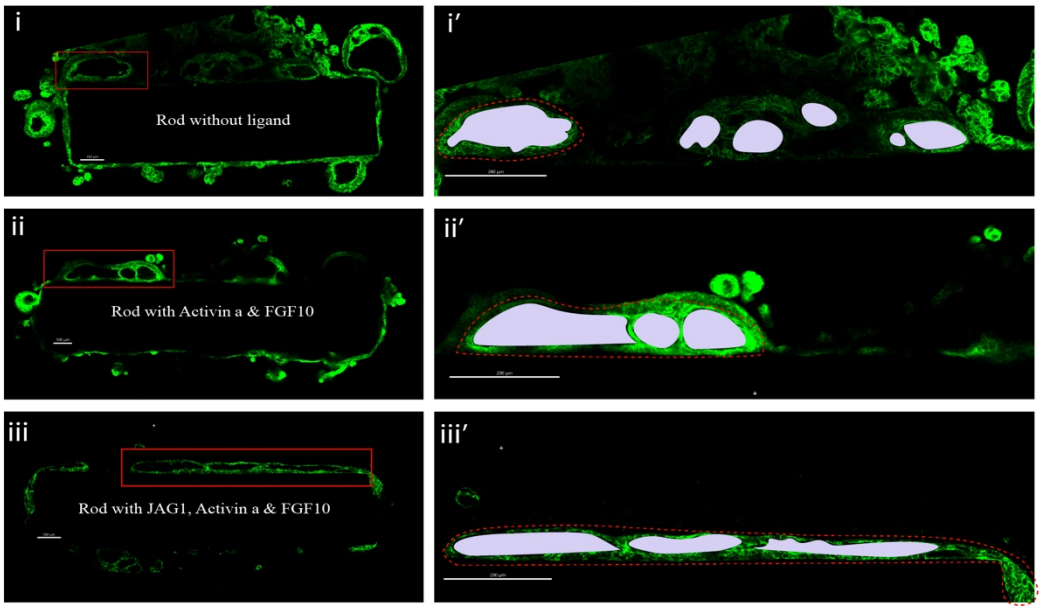

Figure 4

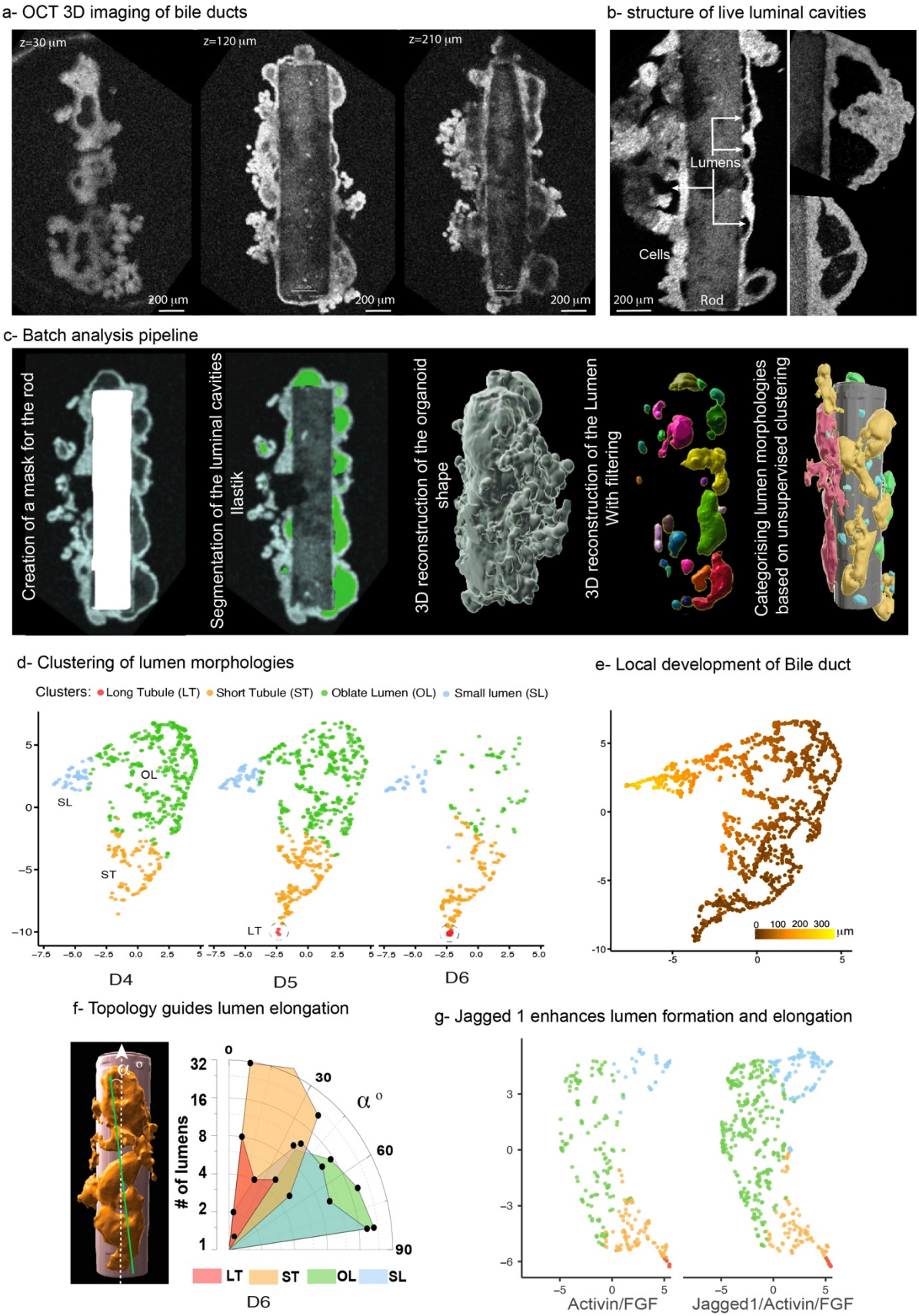
a- OCT 3D imaging of bile ducts
z=30 µm
z=120 µm
z=210 µm
200 µm
200 µm
200 µm
b- structure of live luminal cavities
Lumens
Cells
Rod
200 µm
c- Batch analysis pipeline
Creation of a mask for the rod
Segmentation of the luminal cavities
Ilastik
3D reconstruction of the organoid shape
3D reconstruction of the Lumen
With filtering
Categorising lumen morphologies based on unsupervised clustering
d- Clustering of lumen morphologies
Clusters: Long Tubule (LT) Short Tubule (ST) Oblate Lumen (OL) Small lumen (SL)
OL
SL
ST
LT
D4
D5
D6
e- Local development of Bile duct
0 100 200 300 µm
f- Topology guides lumen elongation
α °
# of lumens
LT ST OL SL
D6
g- Jagged 1 enhances lumen formation and elongation
Activin/FGF
Jagged1/Activin/FGF

Figure 5

Figure Captions:

Figure 1: a. Model of bile duct development in mouse and presumably in human **b.** Schematic representation of the functionalization of the rod bio scaffold **c.** Characterization of the rod biofunctionalization in terms of grafting efficiency of Activin A and its localization on the rod. Phase contrast image of a single GelMa rod and overview of a 96 well plate with a single bio scaffold per well. **d.** Culture protocol from hiPSCs differentiation (2D) to the maturation of the hPPAo (3D).

Figure 2: a.i Single-plane confocal image of the cellular distribution at Day 1 along the bioscaffold (µrod). Cholangiocytes (marked by E-cadherin) line the rod and are sheathed by hepatoblasts (marked by HNF4α) **ii** 3D volume rendering of the cellular distribution **iii** Selective 3D representation of the cell distribution within 20 µm of the rod surface **iv** Transversal view of the cellular distribution **b.** Single-plane image of the cellular distribution at Day 6 with a close-up of the bile duct luminal cavity **c.** Single-plane image showing laminin deposition forming a basal layer for the bile duct **d.** Immunostaining for various cholangiocyte markers **e.** Immunostaining for various hepatoblast and hepatocyte markers.

Figure 3: a. 3' 10X single-cell RNA-seq of hPPAo at Day 6 **b.** Schematic of the typical spatial distribution of the different cell types within the hPPAo at Day 6 **c.** Single-plane confocal image showing the principal marker for each cell type; note the localization of endothelial cells as the first monolayer around the rods and as lumens adjacent to the bile ducts **d.** 3' 10X single-cell RNA-seq at Day 1 and Day 6 showing the maturation of the cellular populations; Log2 fold-change expression levels of the principal genes overexpressed in each cell type **e.** Number of cells per cell type at Day 1 and Day 6.

Figure 4: a. Dependence of the degree and spatial organization of cholangiocytes at Day 1 on the juxtacrine signaling environment (no growth factors on the rods, Activin A + FGF10, or Activin A + FGF10 + Jag1). 3D volume rendering of cholangiocytes in the first cellular layer on the rod surface. Cylindrical unwrapping of raw intensity confocal images **b.** Quantification of morphological signatures derived from the cylindrical projections: **i** fraction of cholangiocytes in the first monolayer **ii** number of disconnected clusters **iii** area of individual clusters **c.** UMAPs from 3' 10X single-cell RNA-seq comparing cell populations under each juxtacrine signaling condition, showing no significant differences **d.** Variability of bile duct morphologies under different juxtacrine signaling conditions at Day 6; rods without growth factors generate discontinuous spherical lumens, Activin A + FGF10 induces longer, compartmentalized tubular ducts, and Activin A + FGF10 + Jag1 generates long, connected tubular ducts spanning the entire rod length.

Figure 5: a. Optical sections of a 3D hPPAo using Optical Coherence Tomography (OCT); the cellular, rod, and luminal regions are clearly distinguishable **b.** High-resolution OCT close-up of cellular septa within elongated tubular bile ducts (indicated by yellow arrows), indicative of connections between different compartments **c.** Schematic of the batch analysis process: establishment of a mask for the rod interior, training and detection of luminal cavities using Ilastik, 3D reconstruction of the hPPAo volume, 3D segmentation of individual lumens, followed by unsupervised clustering of lumen morphologies **d.** Clustering (UMAPs) of seven morphological features of lumens comparing Day 4, Day 5, and Day 6; the long bile ducts (around one per organoid), appear as a small distinct cluster (red) **e.** Heat map of the distance of each lumen cluster relative to the rod surface; longer lumens tend to be located closer to the

rod **f.** Radial histogram of the distribution of angles between the long axis of the ducts and the rod axis for each cluster type; although the angle contributes to clustering, elongated lumens consistently align with the rod's main axis **g.** Clustering (UMAPs) of seven morphological features of lumens comparing Activin A + FGF10 and Activin A + FGF10 + Jag1 conditions; Activin A + FGF10 + Jag1 leads to an overall increase in the number of lumens, with a higher proportion of long tubular structures

Acknowledgments:
VV acknowledges support from MBI core funding, CALIPSO grant NRF2019-THE002-0007, and Chaire d'Excellence AMIDEX 2ORGASRH. The hIPSCS used in this work were a kind gift from S.Tamir Rachid (Imperial College UK)

Conflict of interest

The authors declare no conflict of interests

Material and Methods

Fabrication and functionalization of GelHep µrods

GelHep µrods were fabricated using TYGON tubing (0.5 mm inner diameter; Cole-Parmer). A precursor solution was prepared by mixing 5% (w/v) GelMA with 2.5% (w/v) heparin sulfate at a 2:1 ratio. All materials in contact with the µrods (tubing and containers) were passivated with 2% (w/v) Pluronic F-127 (Sigma-Aldrich) for 1 h at room temperature and rinsed extensively with distilled water. The GelHep solution was prewarmed, degassed, and injected into the passivated tubing using a syringe, followed by UV crosslinking (50% power, 10 min total, with one 5-min interval).

Following crosslinking, the tubing was cut into ~1–1.5 mm segments and subjected to graded ethanol dehydration up to 90% (v/v) to facilitate release of the rods. Tubes were then incubated overnight at 4 °C in a shaking incubator to allow slow rod release. The following day, rods were collected and chemically stabilized by crosslinking in 90% ethanol with 2 mg/ml EDC and 0.48 mg/ml NHS for 6 h at room temperature. After crosslinking, rods were stored overnight in 70% ethanol.

For ligand coupling, rods were sterilized and preactivated in 2 mM EDC and 5 mM NHS for 15 min at room temperature. Activated rods were incubated with Protein G overnight in PBS to enable ligand immobilization. Rods were subsequently washed with PBS and resuspended with growth factors or ligands at defined concentrations. Growth factors were applied at 5-fold higher concentrations than those used for differentiation protocols, whereas JAG1 was coupled at an optimized density corresponding to ~20 ng per rod. For control conditions, GelHep rods were incubated overnight in PBS without ligands.

Fabrication and functionalization of GelHep µbeads

GelHep µbeads were generated by emulsification. Briefly, 200 µl of GelHep solution [10% (w/v) gelatin and 5% (w/v) heparin sulfate (Sigma-Aldrich) in sterile distilled water] was added to 5 ml of mineral oil containing 2% (v/v) SPAN80 (Sigma-Aldrich) and stirred at low speed for 5 min. The emulsion was cooled on ice for 10 min, after which an equal volume of 30% (v/v) ethanol (Sigma-Aldrich) was added. The suspension was centrifuged at 1500 rpm for 5 min to promote phase separation. The supernatant containing oil and ethanol was discarded, and µbeads were sequentially washed with ethanol solutions of increasing concentration up to 90% (v/v).

During the final 90% ethanol wash, µbeads were crosslinked with EDC (2 mg/ml) and NHS (0.48 mg/ml) for 6 h at room temperature on a rocking platform to stabilize intramolecular bonds. An optional wash with 2% (w/v) BSA (Sigma-Aldrich) was performed to remove residual oil deposits. Beads were then stored in 70% ethanol overnight for sterilization.

For ligand immobilization, µbeads (100 µl suspension) were pelleted by centrifugation at 5000 rpm for 3 min and resuspended in PBS containing growth factors at 5-fold higher concentrations than those used for differentiation protocols. Beads were incubated overnight at 4 °C. For control conditions, GelHep µbeads were incubated overnight in PBS without ligands.

Enzyme-linked immunosorbent assay (ELISA)

Growth factor incorporation into GelHep µrods was quantified using the Quantikine ELISA kit for Activin A (R&D Systems) according to the manufacturer's instructions. Briefly, 100 GelHep µrods were incubated in PBS containing 250 ng/ml Activin A for 24 h at room temperature. Supernatants were collected immediately before incubation and after 24 h to determine the amount of growth factor immobilized onto the µrods.

Measurement of GelHep µrods Elastic modulus

The mechanical properties of GelHep µrods were measured using a NanoWizard IV BioAFM system (JPK Instruments, Germany) in collaboration with Dr. C.T. Lim's group. Prior to measurement, µrods were allowed to swell in PBS for 5 min and affixed to plastic Petri dishes. Indentation measurements were performed on 18 µrods obtained from two independent fabrication batches. A polystyrene bead (45 µm diameter; Novascan Technologies, USA) was attached to a cantilever with a spring constant of 0.17 N/m, and indentations were carried out using a loading force of 5 nN at a speed of 5 µm/s.

Young's modulus values were extracted from approach curves using JPK Data Processing Software (JPK Instruments, Germany), applying the Hertz contact model for a spherical indenter (diameter 45 µm; Poisson's ratio 0.5).

Protein G quantification

Immobilization of Protein G on GelHep µrods was confirmed by antibody binding. Protein G–coupled µrods were incubated with rabbit secondary antibody (1:500 dilution) and washed extensively with PBS to remove unbound antibody. Fluorescence imaging was performed using an Olympus FV3000 NIR confocal microscope, and signal intensity profiles were quantified using ImageJ Intensity Profile Tool.

hiPSC culture

Human induced pluripotent stem cells (hiPSCs; provided by Dr. Tamir Rashid, King's College London) were maintained on Vitronectin XF–coated culture flasks (Nunc™ EasYFlask™, Thermo Fisher Scientific). Cells were cultured in TeSR-E8 medium (STEMCELL Technologies) with daily medium changes and passaged every 5 days using ReLeSR (STEMCELL Technologies). For passaging, cells were replated as small colonies.

Differentiation protocol

Generation of hepatoblasts from hiPSCs

hiPSCs were differentiated into hepatoblasts following established protocols. Colonies of appropriate size were dissociated with ReLeSR (STEMCELL Technologies) and seeded onto 6-well tissue culture plates (Corning Costar) pre-coated with 0.1% gelatin and mouse embryonic fibroblast (MEF) medium [DMEM (Sigma-Aldrich) supplemented with FBS (Gibco), L-glutamine (Gibco), penicillin–streptomycin (Gibco), and 2-mercaptoethanol

(Gibco)]. Cells were primed in TeSR-E8 medium (STEMCELL Technologies) for 24 h and maintained in a hypoxic incubator at 37 °C with 5% CO_2 and 5% O_2.
Hepatoblast differentiation was induced by sequential addition of growth factors and small molecules in RPMI medium (Sigma-Aldrich) supplemented with penicillin–streptomycin, MEM non-essential amino acids (MEM-NEAA, Life Technologies), and B27 supplement (Life Technologies). The following reagents were applied to target definitive endoderm, foregut, and hepatoblast stages: Activin A (100 ng/ml, R&D Systems), FGF2/bFGF (80 ng/ml, R&D Systems), BMP4 (10 ng/ml, R&D Systems), LY294002 (10 µM, R&D Systems), CHIR99021 (3 µM, R&D Systems), Activin A (50 ng/ml, R&D Systems), SB431542 (10 µM, R&D Systems), and BMP4 (50 ng/ml, R&D Systems).

Differentiation of hepatoblasts to cholangiocytes using ligand-immobilized µrods
On day 13 of differentiation, hepatoblasts were dissociated into a single-cell suspension using Accutase (STEMCELL Technologies). Cells (10,000 per rod) were seeded in low-attachment 96-well plates (Corning) together with one GelHep µrod per well in a total volume of 200 µl RPMI/B27 medium supplemented with Y-27632. Cells were allowed to self-aggregate with the rods for 24 h, after which medium was replenished daily for 6 days in the absence of soluble growth factors or Y-27632.

Differentiation of hepatoblasts to cholangiocytes using ligand-immobilized µbeads
For µbead-based induction, hepatoblasts at day 13 were dissociated into a single-cell suspension using Accutase (STEMCELL Technologies). Cells were seeded in low-attachment round-bottom 96-well plates at a bead-to-cell ratio of 1:10 in 200 µl RPMI/B27 medium supplemented with Y-27632. Self-aggregation was allowed for 24 h, followed by daily medium changes for 6 days without soluble growth factors or Y-27632.

Immunostaining
3D samples were fixed in 4% paraformaldehyde for 20 min at room temperature or in a 37 °C incubator, followed by permeabilization in 1% Triton X-100 in PBS overnight at 4 °C. Samples were then incubated in blocking buffer [2% (w/v) BSA and 1% Triton X-100 in PBS] overnight at 4 °C, followed by incubation with primary antibodies diluted in antibody buffer [2% (w/v) BSA and 0.2% Triton X-100 in PBS] for 48 h at 4 °C.

Primary antibodies used were: HNF4A (rabbit, Cell Signaling Technology), AFP (mouse, Abcam), cytokeratin 7 (rabbit, Abcam), SOX17 (goat, R&D Systems), SOX9 (rabbit, Cell Signaling Technology), E-cadherin (mouse, BD Biosciences), and laminin (rabbit, Sigma-Aldrich). Samples were washed twice in washing buffer [3% (w/v) NaCl and 0.2% Triton X-100 in PBS] at room temperature for 1 h, followed by overnight incubation at 4 °C.

Secondary antibody incubation was performed for 24 h at 4 °C in the presence of DAPI (0.5 µg/ml; Invitrogen) and ATTO-565 phalloidin (ATTO-TEC). Washing was carried out as described for primary antibodies. Samples were cleared in prewarmed RapiClear 1.52 (Sunjin Lab) and mounted using spacers (0.2 mm for organoids with µbeads; 0.5 mm for organoids with µrods) before sealing with a coverslip. Immunofluorescence images were acquired using an Olympus FV3000 NIR confocal microscope.

Live-cell imaging by bright-field microscopy
For live imaging, organoids were transferred from low-attachment round-bottom 96-well plates into low-attachment glass-bottom 96-well plates. Imaging was performed using a Zeiss Celldiscoverer 7 widefield microscope, with images acquired once per hour over a 3-day period.

Image analysis and quantification
3D rendering was carried out using IMARIS (v10.1, Bitplane) and Fiji (ImageJ). Graphs and statistical analyses were generated using Origin (OriginLab).

Optical coherence tomography (OCT) imaging
OCT imaging was performed in collaboration with Dr. Brendan F. Kennedy (Harry Perkins Institute). Bile duct organoids cultured in U-bottom 96-well plates were suspended in PBS and imaged using a benchtop spectral-domain OCT system (Telesto III OCTG, Thorlabs, USA). The system was equipped with a motorized stage and an objective lens (LSM02, Thorlabs) providing a lateral field of view of 4.2 × 4.2 mm and a lateral resolution of 4.8 μm in air.

Single-cell RNA sequencing
Single-cell suspensions were prepared from 50 organoids by dissociation with Accutase (STEMCELL Technologies) for 20 min. The aqueous layer containing cells was collected, leaving rods settled at the bottom, and passed through a 40 μm cell strainer to generate uniform suspensions. Following centrifugation, cells were resuspended in PBS containing 0.1% BSA. Libraries were prepared using the 10x Genomics platform, and sequencing data were processed with Cell Ranger to generate count matrices.

Downstream analysis was performed using Seurat v5. Count matrices were converted into Seurat objects, and quality control filters were applied to remove cells with >10,000 or <2,000 detected genes, >100,000 or <5,000 total molecules, or >10% mitochondrial reads. Doublets were identified and removed using the *scDblFinder* package. Data were normalized using the NormalizeData function in Seurat, and 2,000 highly variable genes were selected for further analysis. Datasets were scaled, and principal component analysis (PCA) was applied for linear dimensionality reduction. Clustering was performed on up to 30 PCs at a resolution of 0.5, and non-linear dimensionality reduction was performed using UMAP. Clusters were annotated manually based on expression of canonical marker genes (Table 7.1).

Optical coherence tomography

The cell-laden scaffold samples were imaged using a fiber-based spectral-domain OCT system (TEL220, Thorlabs Inc., USA). The focussed optical beam in the OCT system illuminates the sample with nonionizing, near-infrared light with a central wavelength of 1300 nm and a spectral bandwidth of 170 nm. The OCT scan lens used (LSM02, Thorlabs Inc., USA) has a numerical aperture of 0.11. The backscattered light returning from the sample is detected on a spectrometer and the time delay between the sample and reference arms of a Michelson interferometer is used to reconstruct a depth profile (A-scan) of sample backscattering. The OCT beam was scanned laterally to acquire two-dimensional (B-scan) and three-dimensional images of the sample, with experimentally measured axial and lateral resolutions of 4.8 μm and 4.4 μm, respectively, to 1−2 mm in depth. Each sample was scanned while submerged in cell media in a well of a 96-well plate. Scans comprised 1,000 A-scans per B-scan, and 1,000 B-scans per volume over a 2×2 mm (xy) lateral field-of-view, resulting in a lateral sampling density of 2 μm per voxel. The axial sampling density, set by the specifications of the spectrometer, was 2.5 μm per voxel. The A-scan acquisition frequency was 50 kHz, resulting in an OCT volume acquisition time of approximately 20 seconds.

Step	Description	Parameters / Thresholds
Cell dissociation	Organoids dissociated with Accutase; rods left at the bottom	20 min incubation
Filtration	Cells passed through a 40 µm strainer	—
Resuspension	Cells in PBS + 0.1% BSA	—
Library preparation & sequencing	10x Genomics platform	—
Initial processing	Cell Ranger used to generate count matrix	—
Seurat object creation	Count matrix converted into Seurat object	—
Filtering: gene counts	Remove cells with too few or too many genes	<2,000 or >10,000 genes
Filtering: molecule counts	Remove cells with extreme total molecule counts	<5,000 or >100,000 molecules
Filtering: mitochondrial reads	Remove cells with high mitochondrial content	>10% mitochondrial reads
Doublet removal	Identify and remove doublets	*scDblFinder* package
Normalization	Normalize gene expression	NormalizeData function, Seurat
Highly variable gene selection	Identify genes for downstream analysis	Top 2,000 genes
Scaling	Scale datasets to reduce technical variation	—
Linear dimensionality reduction	Principal component analysis (PCA)	Up to 30 PCs used for clustering
Clustering	Identify cell clusters	Resolution = 0.5
Non-linear dimensionality reduction	UMAP embedding	—
Cluster annotation	Manual annotation using canonical marker genes	See Table 7.1

Reference List

[1] P. Van Eyken, R. Sciot, F. Callea, K. V. D. Steen, P. Moerman, and V. J. Desmet, "The development of the intrahepatic bile ducts in man: A keratin-immunohistochemical study," *Hepatology,* vol. 8, no. 6, pp. 1586-1595, 1988, doi: 10.1002/hep.1840080619.

[2] V. J. Desmet, "Congenital Diseases of Intrahepatic Bile Ducts: Variations on the Theme "Ductal Plate Malformation"," *Hepatology,* vol. 16, no. 4, pp. 1069-1083, 1992, doi: 10.1002/hep.1840160434.

[3] F. Clotman *et al.*, "Control of liver cell fate decision by a gradient of TGF beta signaling modulated by Onecut transcription factors," (in eng), *Genes Dev,* vol. 19, no. 16, pp. 1849-54, Aug 15 2005, doi: 10.1101/gad.340305.

[4] J. J. Hofmann, A. C. Zovein, H. Koh, F. Radtke, G. Weinmaster, and M. L. Iruela-Arispe, "Jagged1 in the portal vein mesenchyme regulates intrahepatic bile duct development: insights into Alagille syndrome," (in eng), *Development,* vol. 137, no. 23, pp. 4061-72, Dec 2010, doi: 10.1242/dev.052118.

[5] A. Antoniou *et al.*, "Intrahepatic bile ducts develop according to a new mode of tubulogenesis regulated by the transcription factor SOX9," (in eng), *Gastroenterology,* vol. 136, no. 7, pp. 2325-33, Jun 2009, doi: 10.1053/j.gastro.2009.02.051.

[6] Y. Takashima, M. Terada, M. Kawabata, and A. Suzuki, "Dynamic three-dimensional morphogenesis of intrahepatic bile ducts in mouse liver development," (in eng), *Hepatology,* vol. 61, no. 3, pp. 1003-11, Mar 2015, doi: 10.1002/hep.27436.

[7] G. Gouysse *et al.*, "Relationship between vascular development and vascular differentiation during liver organogenesis in humans," *Journal of Hepatology,* vol. 37, no. 6, pp. 730-740, 2002/12/01/ 2002, doi: https://doi.org/10.1016/S0168-8278(02)00282-9.

[8] L. Fabris *et al.*, "Epithelial expression of angiogenic growth factors modulate arterial vasculogenesis in human liver development," *Hepatology,* vol. 47, no. 2, pp. 719-728, 2008.

[9] Y. Guan *et al.*, "Human hepatic organoids for the analysis of human genetic diseases," (in eng), *JCI Insight,* vol. 2, no. 17, Sep 7 2017, doi: 10.1172/jci.insight.94954.

[10] S. P. Harrison *et al.*, "Scalable production of tissue-like vascularized liver organoids from human PSCs," *Experimental & Molecular Medicine,* vol. 55, no. 9, pp. 2005-2024, 2023/09/01 2023, doi: 10.1038/s12276-023-01074-1.

[11] T. Takebe *et al.*, "Vascularized and functional human liver from an iPSC-derived organ bud transplant," *Nature,* vol. 499, no. 7459, pp. 481-484, 2013/07/01 2013, doi: 10.1038/nature12271.

[12] F. Sampaziotis, M. C. de Brito, I. Geti, A. Bertero, N. R. Hannan, and L. Vallier, "Directed differentiation of human induced pluripotent stem cells into functional cholangiocyte-like cells," (in eng), *Nat Protoc,* vol. 12, no. 4, pp. 814-827, Apr 2017, doi: 10.1038/nprot.2017.011.

[13] M. Ogawa *et al.*, "Directed differentiation of cholangiocytes from human pluripotent stem cells," (in eng), *Nat Biotechnol,* vol. 33, no. 8, pp. 853-61, Aug 2015, doi: 10.1038/nbt.3294.

[14] N. Dianat *et al.*, "Generation of functional cholangiocyte-like cells from human pluripotent stem cells and HepaRG cells," (in eng), *Hepatology,* vol. 60, no. 2, pp. 700-14, Aug 2014, doi: 10.1002/hep.27165.

[15] M. Ogawa *et al.*, "Generation of functional ciliated cholangiocytes from human pluripotent stem cells," *Nature Communications,* vol. 12, no. 1, p. 6504, 2021/11/11 2021, doi: 10.1038/s41467-021-26764-0.

[16] M. N. B. Ramli *et al.*, "Human Pluripotent Stem Cell-Derived Organoids as Models of Liver Disease," *Gastroenterology,* vol. 159, no. 4, pp. 1471-1486.e12, 2020, doi: 10.1053/j.gastro.2020.06.010.

[17] A. Funfak, L. Bouzhir, E. Gontran, N. Minier, P. Dupuis-Williams, and S. Gobaa, "Biophysical Control of Bile Duct Epithelial Morphogenesis in Natural and Synthetic Scaffolds," (in eng), *Front Bioeng Biotechnol,* vol. 7, p. 417, 2019, doi: 10.3389/fbioe.2019.00417.

[18] G. Sorrentino *et al.*, "Mechano-modulatory synthetic niches for liver organoid derivation," *Nature Communications,* vol. 11, no. 1, p. 3416, 2020/07/10 2020, doi: 10.1038/s41467-020-17161-0.

[19] K. B. Kaylan *et al.*, "Spatial patterning of liver progenitor cell differentiation mediated by cellular contractility and Notch signaling," (in eng), *Elife,* vol. 7, Dec 27 2018, doi: 10.7554/eLife.38536.

[20] M. Rizwan *et al.*, "Photochemically Activated Notch Signaling Hydrogel Preferentially Differentiates Human Derived Hepatoblasts to Cholangiocytes," *Advanced Functional Materials,* vol. 31, no. 5, p. 2006116, 2021, doi: https://doi.org/10.1002/adfm.202006116.

[21] S. D. Gentile, A. P. Kourouklis, H. Ryoo, and G. H. Underhill, "Integration of Hydrogel Microparticles With Three-Dimensional Liver Progenitor Cell Spheroids," (in eng), *Front Bioeng Biotechnol,* vol. 8, p. 792, 2020, doi: 10.3389/fbioe.2020.00792.

[22] E. Gontran *et al.*, "Self-Organogenesis from 2D Micropatterns to 3D Biomimetic Biliary Trees," *Bioengineering,* vol. 8, no. 8, p. 112, 2021.

[23] F. J. M. Roos *et al.*, "Human branching cholangiocyte organoids recapitulate functional bile duct formation," (in eng), *Cell Stem Cell,* vol. 29, no. 5, pp. 776-794.e13, May 5 2022, doi: 10.1016/j.stem.2022.04.011.

[24] E. Carolina *et al.*, "Generation of human iPSC-derived 3D bile duct within liver organoid by incorporating human iPSC-derived blood vessel," *Nature Communications,* vol. 15, no. 1, p. 7424, 2024/08/28 2024, doi: 10.1038/s41467-024-51487-3.

[25] S. J. I. Blackford *et al.*, "Validation of Current Good Manufacturing Practice Compliant Human Pluripotent Stem Cell-Derived Hepatocytes for Cell-Based Therapy," (in eng), *Stem Cells Transl Med,* vol. 8, no. 2, pp. 124-137, Feb 2019, doi: 10.1002/sctm.18-0084.

[26] B. T. Wesley *et al.*, "Single-cell atlas of human liver development reveals pathways directing hepatic cell fates," *Nature Cell Biology,* vol. 24, no. 10, pp. 1487-1498, 2022/10/01 2022, doi: 10.1038/s41556-022-00989-7.

[27] L. Yang, W. H. Wang, W. L. Qiu, Z. Guo, E. Bi, and C. R. Xu, "A single-cell transcriptomic analysis reveals precise pathways and regulatory mechanisms underlying hepatoblast differentiation," (in eng), *Hepatology,* vol. 66, no. 5, pp. 1387-1401, Nov 2017, doi: 10.1002/hep.29353.

[28] W. Yang *et al.*, "Single-Cell Transcriptomic Analysis Reveals a Hepatic Stellate Cell-Activation Roadmap and Myofibroblast Origin During Liver Fibrosis in Mice," (in eng), *Hepatology,* vol. 74, no. 5, pp. 2774-2790, Nov 2021, doi: 10.1002/hep.31987.

[29] X. Wang *et al.*, "Comparative analysis of cell lineage differentiation during hepatogenesis in humans and mice at the single-cell transcriptome level," *Cell Research,* vol. 30, no. 12, pp. 1109-1126, 2020/12/01 2020, doi: 10.1038/s41422-020-0378-6.

[30] S. A. MacParland *et al.*, "Single cell RNA sequencing of human liver reveals distinct intrahepatic macrophage populations," *Nature Communications,* vol. 9, no. 1, p. 4383, 2018/10/22 2018, doi: 10.1038/s41467-018-06318-7.

[31] N. Tanimizu *et al.*, "Intrahepatic bile ducts are developed through formation of homogeneous continuous luminal network and its dynamic rearrangement in mice," (in eng), *Hepatology,* vol. 64, no. 1, pp. 175-88, Jul 2016, doi: 10.1002/hep.28521.

[32] E. E. Sparks, K. A. Huppert, M. A. Brown, M. K. Washington, and S. S. Huppert, "Notch signaling regulates formation of the three-dimensional architecture of intrahepatic bile ducts in mice," (in eng), *Hepatology,* vol. 51, no. 4, pp. 1391-400, Apr 2010, doi: 10.1002/hep.23431.

[33] S. Benhamouche-Trouillet *et al.*, "Proliferation-independent role of NF2 (merlin) in limiting biliary morphogenesis," *Development,* vol. 145, no. 9, 2018, doi: 10.1242/dev.162123.

[34] P. Van Liedekerke, L. Gannoun, A. Loriot, T. Johann, F. P. Lemaigre, and D. Drasdo, "Quantitative modeling identifies critical cell mechanics driving bile duct lumen formation," (in eng), *PLoS Comput Biol,* vol. 18, no. 2, p. e1009653, Feb 2022, doi: 10.1371/journal.pcbi.1009653.

[35] M. J. Lee *et al.*, "Long-term three-dimensional high-resolution imaging of live unlabeled small intestinal organoids via low-coherence holotomography," *Experimental & Molecular Medicine,* vol. 56, no. 10, pp. 2162-2170, 2024/10/01 2024, doi: 10.1038/s12276-024-01312-0.

[36] R. Morishita *et al.*, "Label-free intratissue activity imaging of alveolar organoids with dynamic optical coherence tomography," (in eng), *Biomed Opt Express,* vol. 14, no. 5, pp. 2333-2351, May 1 2023, doi: 10.1364/boe.488097.